Journal of Solid State Chemistry 275 (2019) 159–166

Contents lists available at ScienceDirect

Journal of Solid State Chemistry

journal homepage: www.elsevier.com/locate/jssc

Influence of zinc substitution with cobalt on thermal behaviour, structure and morphology of zinc ferrite embedded in silica matrix

Thomas Dippong [a], Firuţa Goga [b], Erika-Andrea Levei [c,*], Oana Cadar [c]

[a] Technical University of Cluj-Napoca, North University Center of Baia Mare, Department of Chemistry and Biology, 76 Victoriei Street, 430122 Baia Mare, Romania
[b] Babes-Bolyai University, Faculty of Chemistry and Chemical Engineering, 11 Arany Janos Street, 400028 Cluj-Napoca, Romania
[c] INCDO-INOE 2000, Research Institute for Analytical Instrumentation, 67 Donath Street, 400293 Cluj-Napoca, Romania

ARTICLE INFO

Keywords:
Zinc-cobalt ferrite
Thermal decomposition
Sol-gel synthesis
Activation energy

ABSTRACT

The influence of Zn^{2+} substitution with Co^{2+} on the thermal behaviour, morphology and structure of $ZnFe_2O_4$ was studied. The $ZnFe_2O_4$ and Co-substituted $ZnFe_2O_4$ ($Co_{0.3}Zn_{0.7}Fe_2O_4$ and $Co_{0.7}Zn_{0.3}Fe_2O_4$) nanoparticles embedded in SiO_2 matrix were synthesized by a modified sol-gel method. The thermal analysis revealed the formation of Zn-, Fe- and Co-succinate precursors at 130–200 °C and their decomposition to ferrites at 220–400 °C. Fourier transformed infrared spectroscopy confirmed the formation of succinates and their decomposition into ferrites. Isotherms were used to calculate the rate constants for the decomposition of succinates to ferrites and the activation energy for each ferrite. The nanocrystallites have cubic spinel structure and an average diameter of 12–31 nm. At 1000 °C, for $ZnFe_2O_4/SiO_2$ gel, X-ray diffraction (XRD) revealed a main ($ZnFe_2O_4$) and two secondary (Zn_2SiO_4 and SiO_2) phases. By partially substitution ($Co_{0.3}Zn_{0.3}Fe_2O_4/SiO_2$ gel), the secondary phases disappear, XRD revealing only the presence of mixed Zn-Co ferrite. Due to presence of non-magnetic SiO_2 matrix, nearly spherical and non-agglomerated nanoparticles were showed by transmission and scanning electron microscopy. Ferrites are coloured in dark brown to black shades and can be used as ceramic pigments.

1. Introduction

Recently, a wide range of synthetic nano-materials were developed to answer the demands of various high-tech industrial fields for materials with special properties [1–3]. Among them, metal-organic frameworks offer excellent properties for photocatalysis, gas storage, drug delivery and trace metal ion sensing, bimetallic alloy nanoparticles are promising photodegradation agents for various pollutants, while ferrites have applications in water treatment, data storage, sensors, catalysis and drug delivery [4–8].

Due to its biocompatibility, porosity, structure and morphology, magnetic and adsorbing properties, $ZnFe_2O_4$ has received considerable attention for its potential applications in numerous fields such are hyperthermia, anti-cancer drug sensor and gas sensing [9,10]. Presently, $CoFe_2O_4$ is used for magnetic recording and magnetic fluids, whereas $ZnFe_2O_4$ as catalyst [11]. The Co-Zn ratio in the ferrite structure, the preparation method, the particle size, shape and size distribution significantly influence the nanoparticle's properties [12,13]. In this regard, the partial Zn substitution with Co changes the ferrite properties, broadening its field of application by improving its structural, magnetic and electrical properties [14]. Moreover, Zn is easily incorporable into the lattice of $CoFe_2O_4$ due to the comparable sizes of Zn^{2+} and Co^{2+} ions [11,13]. Zn-substituted $CoFe_2O_4$ nanoparticles have attracted great interest because of their interesting electrical, optical and magnetic properties and possibilities for many high-tech applications, such as electronic devices and ferrofluids, diagnostic and cancer therapy, drug delivery, microwave devices, crystal photonics, data and energy storage, sensors, supercapacitors, photomagnetic devices, photocatalysis [15–18].

The high permeability in the radio frequency region, electrical resistivity, mechanical hardness and chemical stability of nano-ferrites have encouraged the use of different synthesis methods in order to optimize the morphology, porosity and crystallite size [12,16]. Zn-Co ferrites were prepared through co-precipitation, sol-gel, citrate precursor, hydrothermal, solvothermal, microemulsion, ceramic, forced hydrolysis, microwave and auto-combustion, reverse micelle, ball milling and thermal decomposition methods [18–22]. The thermal method is one of the most suitable technique used for the preparation of ferrite nanoparticles with appropriate stoichiometric control, uniform particle size distribution and relatively short processing time at lower temperatures [10,22]. The sol-gel method is a facile, cost-effective chemical approach

* Corresponding author.
E-mail address: erika.levei@icia.ro (E.-A. Levei).

https://doi.org/10.1016/j.jssc.2019.04.011
Received 1 March 2019; Received in revised form 4 April 2019; Accepted 9 April 2019
Available online 15 April 2019

to obtain reproducible stoichiometric compositions with high yield, suitable for the large-scale production of ferrites with desired microstructure, shape, size and chemical homogeneity compared to the traditional ceramic methods [13]. $ZnFe_2O_4$ and Zn-substituted $CoFe_2O_4$ nanoparticles incorporated into metallic or polymeric matrix may change surface roughness, electrolytic activity or mechanical properties [23].

The colouring of ceramics is based on the addition of dyes or pigments. The ceramic pigments are generally inorganic oxides powders that give a stable colour to glazes, at high temperatures. The colour of pigments depends on the presence of chromophore ions (transition metal) in an inert matrix (oxidic systems). The black pigments are generally obtained from the mixture or pure metal (Co, Fe, Cr and Ni) oxides. $Co_2Fe_2O_4$ is a black pigment widely used in the ceramic industry because of its excellent chemical and thermal stability [24]. Furthermore, a strong correlation between the ferrite-based pigment colour and annealing temperature was remarked [25].

This paper aims to investigate the thermal and kinetic behaviours of $ZnFe_2O_4$ and Zn-substituted $CoFe_2O_4$ in isotherm and non-isotherm conditions. The thermal stability and phase formations were investigated by thermal analysis and Fourier transformed infrared (FT-IR) spectroscopy. The obtained nanoparticles were characterized by X-ray diffraction (XRD), transmission electron microscopy (TEM) and scanning electron microscopy (SEM). The specific surface area of nanoparticle was determined using the Brunauer–Emmett–Teller (BET) method. The Co/Zn/Fe ratio in ferrites was confirmed by inductively coupled plasma optical emission spectrometry (ICP-OES) and energy-dispersive X-ray spectroscopy (EDX).

2. Experimental procedure

Zinc ferrite ($ZnFe_2O_4$) and Co-substituted $ZnFe_2O_4$ ($Co_{0.3}Zn_{0.7}Fe_2O_4$ and $Co_{0.7}Zn_{0.3}Fe_2O_4$) nanoparticles embedded in SiO_2 matrix were obtained by sol-gel method. For synthesis, analytical grade (Merck) reagents were used without further purification. The sols were prepared at room temperature, by mixing nonahydrate ferric nitrate ($Fe(NO_3)_3{\cdot}9H_2O$), hexahydrate cobalt nitrate ($Co(NO_3)_2{\cdot}6H_2O$) and hexahydrate zinc nitrate ($Zn(NO_3)_2{\cdot}6H_2O$) with 1,4 butanediol (1,4-BD) and tetraethylorthosilicate (TEOS) in aqueous ethanolic solution. During synthesis, the following molar ratios were used: Fe:Zn = 2:1 ($ZnFe_2O_4/SiO_2$), Co:Zn:Fe = 0.3:0.7:2 ($Co_{0.3}Zn_{0.7}Fe_2O_4/SiO_2$), Co:Zn:Fe = 0.7:0.3:2 ($Co_{0.7}Zn_{0.3}Fe_2O_4/SiO_2$) and NO_3^-:1.4BD:TEOS = 1:1:1. The obtained solutions were stirred for 30 min and kept at room temperature until gelation. After gelation, the gels were grinded, dried at 40 °C (4 h) and 200 °C (4 h) and annealed at 1000 °C (4 h).

The thermal stability and the formation and decomposition of succinate precursors were investigated by thermogravimetric (TG) and differential thermal analysis (DTA) using a SDT Q600 type instrument, in air up to 1200 °C at 10 °C/min and alumina standards. The FT-IR spectra were recorded on 1% KBr pellets using a Perkin-Elmer Spectrum BX II spectrometer. The XRD patterns were recorded using a Bruker D8 Advance diffractometer, operating at 40 kV and 40 mA, with CuK_α radiation ($\lambda = 1.5406$ Å) at room temperature. TEM observations carried out on a Hitachi HD2700 electron microscope were used to investigate the size, shape and clustering of nanoparticles, while the particle size distributions were determined using UTHSCSA ImageTool Software. The morphology and dispersion of samples were investigated by SEM using a Hitachi SU8230 microscope. The Zn, Co and Fe content of nanocomposites (NCs) was determined using a Perkin-Elmer Optima 3500 DV ICP-OES, after microwave digestion with aqua regia. The powder colour of NCs annealed at 1000 °C was characterized by determining the CIE-LAB coordinates and recording the absorption spectra in UV-VIS using a Konica Minolta CM -2600D spectrophotometer. The UV–visible absorption spectra were recorded in the range of 200–800 nm with a scan rate of 400 nm/min, using a Jasco V-650 spectrophotometer equipped with an ISV-722 Integrating Sphere. The specific surface area (SSA) of NCs was obtained by N_2 adsorption/desorption measurement, at the liquid nitrogen temperature (−196 °C) using a Sorptomatic 1990 apparatus (Thermo Electron Corporation). The samples were degassed before determination for 4 h at 200 °C and 2Pa pressure, in order to remove the physisorbed impurities from the surface. No variation of pressure was observed during 1 h at the end of the degassing process.

3. Results and discussion

3.1. Thermal stability

The TG and DTA curves reveal the formation of Zn-, Co- and Fe-succinate precursors and their decomposition to $ZnFe_2O_4$, $Zn_{0.7}Co_{0.3}Fe_2O_4$, $Zn_{0.3}Co_{0.7}Fe_2O_4$ in the SiO_2 matrix (Fig. 1a). The DTA curve show 4 processes for $ZnFe_2O_4$. The endothermic effect at 69 °C, with 15% weight loss on the TG curve, corresponds to the evaporation of the adsorbed moisture during preparation, while the endothermic effects at 155 and 220 °C with a weight loss of 22% correspond to the oxidation of 1,4-BD and the formation of Fe- and Zn- succinates, respectively. The strong exothermic effect at 267 °C is assigned to the combustion of the Zn- and Fe-succinates, pyrolytic elimination of organic compounds, residual hydroxyl groups and entrapped gases, with the formation of α-Fe_2O_3 and ZnO, that further forms $ZnFe_2O_4$, with a weight loss of 17% [13]. In case of Zn substitution with Co, the weight loss of the global process slightly increases, the 3 endothermic effects occur at lower temperatures, while the exothermic effect at a slightly higher temperature. Thus, at a Co:Zn = 0.3:0.7 M ratio, the water loss take place at 63 °C (12% weight loss), the formation of Fe-, Co- and Zn -succinate precursors at 139 and 200 °C (36% a weight loss), while the decomposition of succinates at 271 °C (14% weight loss), leading to a mixture of highly reactive amorphous oxides (α-Fe_2O_3, CoO and ZnO), which reacts in situ, forming the spinel oxide ($Co_{0.3}Zn_{0.7}Fe_2O_4$). In case of Co:Zn = 0.7:0.3 M ratio, the water loss take place at 64 °C with a weight loss of 10% on the TG curve, the formation of succinate precursors at 146 and 195 °C with a weight loss of 27%, while the decomposition of precursors with formation of oxidic phase take place in two stages at 259 and 304 °C with a weight loss of 25%.

For all NCs, the DTA curves revealed that the spinels formed up to 400 °C does not suffer any other transformations, suggesting that in the range of 400–1200 °C the obtained NCs exhibit thermal stability. The stability of NCs is also confirmed by the lack of mass loss on the TG curves. The thermal stability up to 1200 °C makes these NCs suitable for applications in the glazed ceramic industry.

The decomposition of succinate precursors in time, under isothermal conditions is presented in Fig. 1b. For all samples, in the first 25 min a rapid weight loss was observed, followed by a slow weight loss up to 200 min. In case of the isotherms at 200 °C, the low weight losses indicate the incomplete decomposition of succinates and formation of ferrites. The isotherms at 300 and 350 °C are similar and show a total weight loss of 60%, suggesting that at this temperature the precursors are completely decomposed and the ferrites are formed.

The rate constant (k) was calculated using the isotherms according to Eq. (1):

$$\frac{dx}{dt} = k(x_o - x)^{2/3} \quad (1)$$

where: dx/dt is the reaction rate, x_o is the initial weight (mg), x is the weight at time t (mg), t is the time (min) and k is the rate constant defined as $k = A\, e^{(-E/RT)}$, where A is the pre-exponential factor, E_a is the activation energy, R is the ideal gas constant, T is the temperature [24,26].

The activation energy (E_a) and pre-exponential factor (A) were calculated according to Arrhenius equation (Eq. (2)) [24,26]:

$$\log k = logA - \frac{E_a}{2.303R} \cdot \frac{1}{T} \quad (2)$$

where: A is the pre-exponential factor, E_a is the activation energy (J/

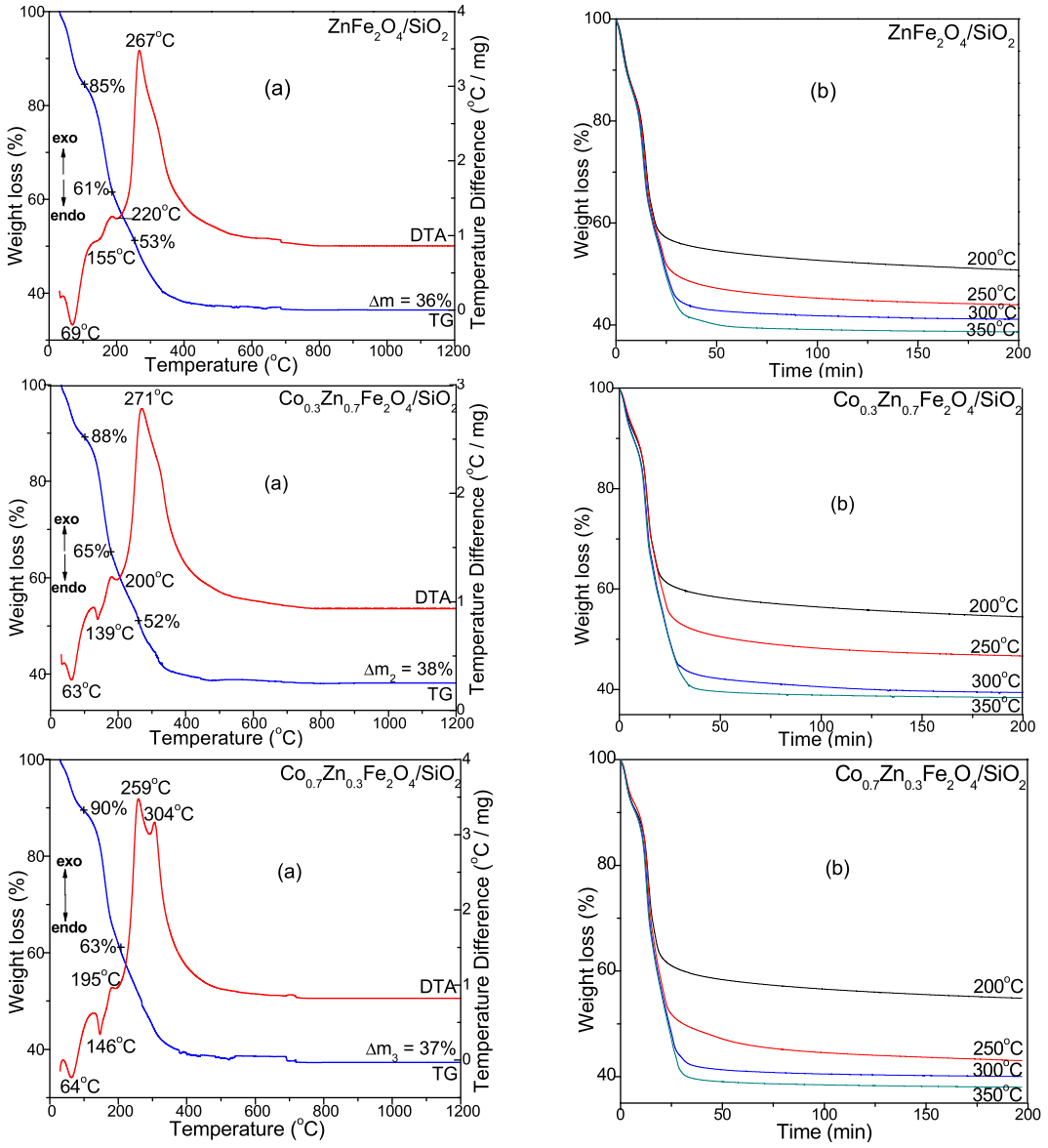

Fig. 1. TG/DTA (a) and TG isotherms at 200, 250, 300, 350 °C (b) of $ZnFe_2O_4$, $Co_{0.3}Zn_{0.7}Fe_2O_4$, $Co_{0.7}Zn_{0.3}Fe_2O_4$ dried at 40 °C.

mol); R is the ideal gas constant (8.314 J/mol·K), T is the temperature (K).

Using the plots of log k vs. 1/T (Fig. 2), the activation energy (E_a) and the pre-exponential factor (A) were calculated from the slope and respectively from the intercept.

The rate constant (Table 1) increases with increasing temperature and increasing Co content in the ferrite structure. The increase of k indicates that the reaction is faster as expected, because more molecules can collide. For all gels, the k values decrease with increasing decomposition time, due to the weight loss during the decomposition process. E_a decreases with increasing Co content in the zinc ferrite, the highest value being found for $ZnFe_2O_4$ (8150 kJ/mol) and the lowest for

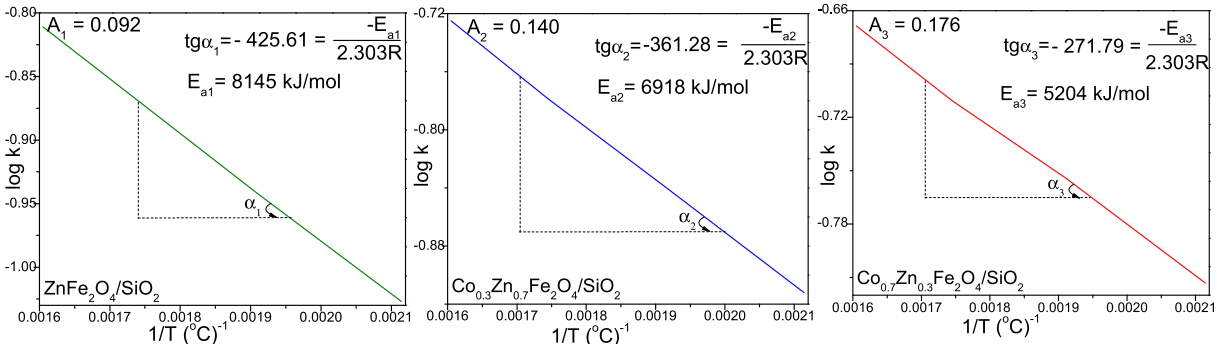

Fig. 2. The plots log k *vs.* 1/T, activation energies (E_a) and pre-exponential factors (A) of $ZnFe_2O_4$, $Co_{0.3}Zn_{0.7}Fe_2O_4$ and $Co_{0.7}Zn_{0.3}Fe_2O_4$.

Table 1
Rate constant values (k), pre-exponential factors (A) and activation energies (E_a) for $ZnFe_2O_4$, $Co_{0.3}Zn_{0.7}Fe_2O_4$, $Co_{0.7}Zn_{0.3}Fe_2O_4$.

Sample	k				A	E_a (kJ/mol)
	200 °C	250 °C	300 °C	350 °C		
$ZnFe_2O_4$	0.094	0.115	0.136	0.155	0.092	8145
$Co_{0.3}Zn_{0.7}Fe_2O_4$	0.122	0.145	0.166	0.187	0.140	6918
$Co_{0.7}Zn_{0.3}Fe_2O_4$	0.154	0.176	0.195	0.215	0.176	5204

$Co_{0.7}Zn_{0.3}Fe_2O_4$ (5204 kJ/mol). A also increases with increasing Co content in the zinc ferrite.

3.2. FT-IR spectroscopy

The FT-IR spectra of $ZnFe_2O_4$, $Co_{0.3}Zn_{0.7}Fe_2O_4$ and $Co_{0.7}Zn_{0.3}Fe_2O_4$/SiO_2 gels dried at 40 and 200 °C, are presented in Fig. 3. At 40 °C, the band at 1380 cm^{-1} is attributed to asymmetric vibration of N-O bond in nitrates, while at 200 °C, this band disappears leading to the formation of bands around 1532 cm^{-1}, suggesting the formation of metal-succinate precursors and the consumption of nitrates up to 200 °C [22,27,28]. At 40 °C, all samples exhibits a broad band at 3390-3419 cm^{-1} assigned to the stretching vibrations of O–H groups in H_2O [22,27,28]. At 200 °C, this band is slightly shifted towards higher wavenumbers (3436-3459 cm^{-1}) suggesting that Co-Zn ferrite, dried at this temperature, is hygroscopic. Another possible explanation for the presence of this absorption band are O-H stretching vibration and Si-OH deformation vibration originated from the hydrolysis of $-Si(OC_2H_5)_4$ [27,29]. The formation of Co-, Zn- and Fe-succinates was confirmed by the bands around at 1532 and 1649 cm^{-1} specific to the asymmetric and symmetric vibration of C═O of COO^- groups [27,29]. The characteristic bands of SiO_2 matrix are also observed: the vibration of Si-O bond at 446–465 cm^{-1}, the vibration of Si-O-Si cyclic structures at 559–562 cm^{-1} (these bands are overlapping the vibration bands of M-O bonds), the symmetric stretching and bending vibration of Si-O-Si chains at 794–800 cm^{-1} (more distinguishable for gels dried at 200 °C, when the SiO_2 matrix is already formed), the vibration of Si-OH bonds at 942–948 cm^{-1} (more distinguishable for gels dried at 40 °C, suggesting the presence of unreacted TEOS) and the stretching vibration of Si-O-Si bonds at 1046–1072 cm^{-1} (confirming the formation of amorphous SiO_2) [22,27,29]. The bands at 559–562 cm^{-1} and 446–465 cm^{-1} are associated with M-O stretching bonds in the tetrahedral and octahedral sites, respectively [28]. The band at 559 cm^{-1} distinguishable only for gels with high Co content at 200 °C could be attributed to the vibration of Co-O bond. At 40 °C, the bands at 2946–2952 and 2876-2888 cm^{-1} are attributed to the asymmetric and symmetric vibration of C-H bond belonging to CH_2 group in 1,4-BD [22,27]. The lack of these bands at 200 °C, may indicate the start of succinate precursors decomposition to Co- and Zn- ferrites.

FT-IR spectra of NCs after annealing at 400 and 1000 °C are shown in Fig. 4. The SiO_2 matrix formation is confirmed by symmetric and asymmetric vibrations at 792-799 cm^{-1} (SiO_4 tetrahedron), 1091-1099 cm^{-1} (Si-O-Si stretching vibrations), the vibration of Si-OH bonds at 901 cm^{-1}, and of Si-O at 446–460 cm^{-1}. The band at 931-932 cm^{-1} is attributed to Fe-O-Si bond, more distinguishable for NCs with high Zn

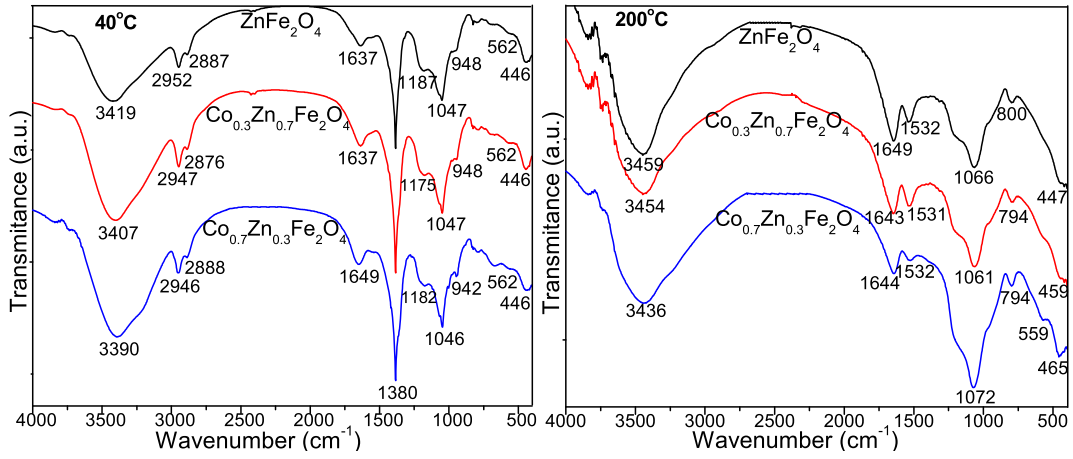

Fig. 3. FT-IR spectra of $ZnFe_2O_4$, $Co_{0.3}Zn_{0.7}Fe_2O_4$ and $Co_{0.7}Zn_{0.3}Fe_2O_4$ at 40 and 200 °C.

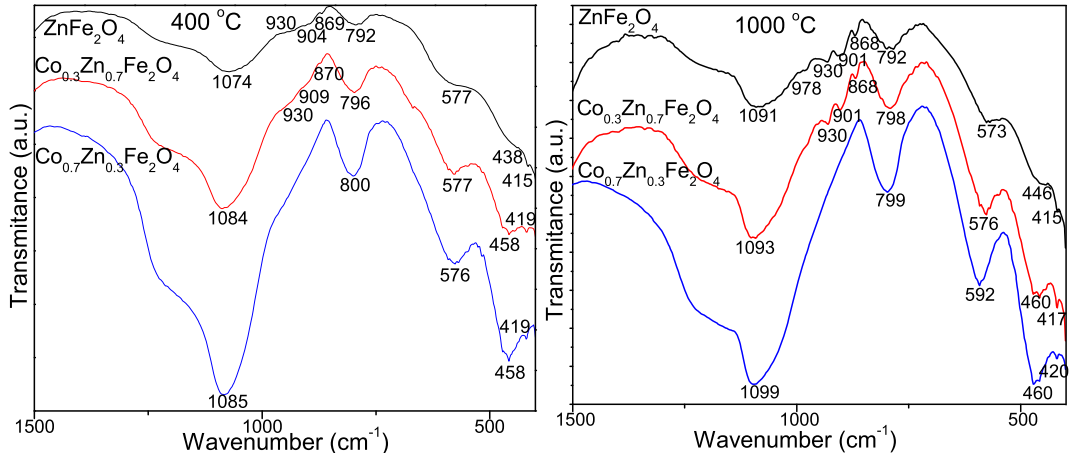

Fig. 4. FT-IR spectra of $ZnFe_2O_4$, $Co_{0.3}Zn_{0.7}Fe_2O_4$, $Co_{0.7}Zn_{0.3}Fe_2O_4$ annealed at 400 and 1000 °C.

content, where XRD indicates the presence of crystalline SiO_2 [19,27]. The absorption band at 573–592 cm^{-1} is assigned to tetrahedral metal complex vibration, while that at 415–420 cm^{-1} is attributed to the octahedral metal complex vibration [13,14,28]. The vibration bands shift with the variation in Zn content probably due to the replacement of Co^{2+} with higher atomic weight and size Zn^{2+} ions [13]. In the FT-IR spectra of $ZnFe_2O_4$ and $Co_{0.3}Zn_{0.7}Fe_2O_4$, the presence of willemite (Zn_2SiO_4) is suggested by the bands at 868 cm^{-1} attributed to symmetric stretching and at 901, 930 and 978 cm^{-1} attributed to asymmetric stretching of SiO_4 [29]. The similar FT-IR spectra of samples annealed at 400 and 1000 °C also suggest the thermal stability of NCs in this temperature range.

3.3. XRD analysis

Fig. 5 presents the XRD patterns of $ZnFe_2O_4$, $Co_{0.3}Zn_{0.7}Fe_2O_4$ and $Co_{0.7}Zn_{0.3}Fe_2O_4$ embedded in SiO_2 matrix, annealed at 400 °C and 1000 °C. At both temperatures the presence of $ZnFe_2O_4$ lines (JCPDS card 16–6205) very close to those of $CoFe_2O_4$ lines (JCPDS card 16–6200) are observed. The Miller indices (111), (220), (311), (222), (400), (422), (511), (440) show a cubic spinel type structure belonging to the Fd-3m space group with very close lattice parameters (isostructural compounds) [30].

The XRD patterns of samples annealed at 400 and 1000 °C show the presence of similar compounds, but those in samples annealed at 400 °C have much lower crystallization degree than those annealed at 1000 °C. For $Co_{0.7}Zn_{0.3}Fe_2O_4$, a single-phase was observed, while for $ZnFe_2O_4$ and $Co_{0.3}Zn_{0.7}Fe_2O_4$, the ferrites are unpurified with Zn_2SiO_4 (JCPDS card 01–1076) and SiO_2 (JCPDS card 89–8935), the substitution of Zn with Co leading to high-purity samples. In gels with high Zn content, the ZnO reacts with SiO_2 resulting Zn_2SiO_4 (willemite). This reaction is thermodynamically more favorable than the reaction between ZnO and Fe_2O_3 with formation of $ZnFe_2O_4$. The low crystallinity at 400 °C indicates the presence of willemite. Furtermore, the presence of the same phases at 400 and 1000 °C also confirms the thermal stability of NCs.

The average diameter of nanocrystallites size (D_C) at 1000 °C was estimated based on the XRD data, using the Scherrer equation [27,31]. The nanocrystallites size (D_C) increases (12 nm - $ZnFe_2O_4$, 20 nm - $Co_{0.3}Zn_{0.7}Fe_2O_4$ 31 nm - $Co_{0.7}Zn_{0.3}Fe_2O_4$), while the diffraction lines intensity decreases with the increase of the Co substitution in Zn ferrite. At 400 °C, due to the low crystallinity degree, the nanocrystallite's size was not estimated.

The activation energy (E_a) of the phase transformation increases while the pre-exponential factor (A) decrease with increasing crystallite size (D_C) (Fig. 6). In both cases, the dependence of activation energy and pre-exponential factor with the crystallite size is linear.

3.4. N_2 adsorption/desorption measurements

For samples annealed at 1000 °C, due to the low amount of adsorbed/desorbed N_2, the N_2 adsorption/desorption measurements did not allow the determination of porosity and specific surface area (SSA). In all cases, the SSA is below the method detection limit (0.5 m^2/g), suggesting non-porous samples. These values are lower than those previously reported for $CoFe_2O_4$ embedded in SiO_2 matrix [32]. These results could be a consequence of the samples agglomeration that limit the absorption of N_2

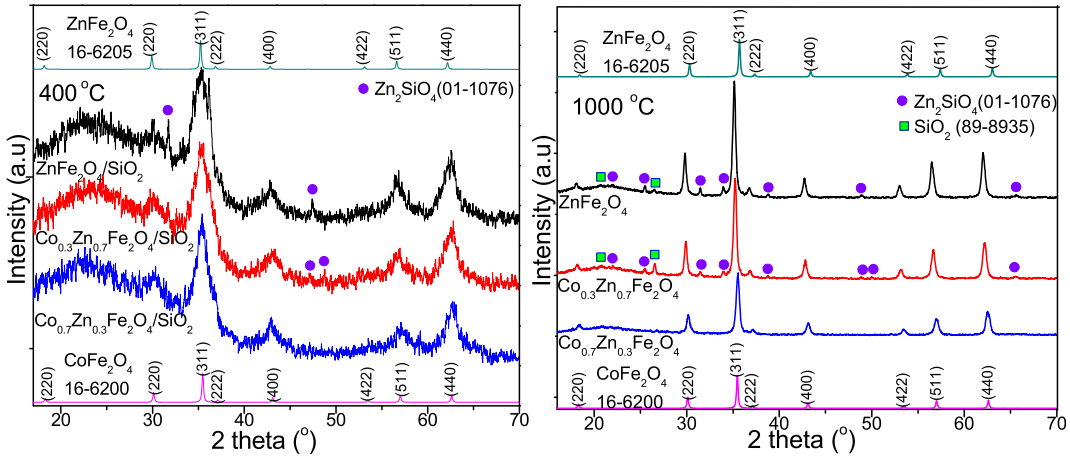

Fig. 5. XRD patterns of $ZnFe_2O_4$, $Co_{0.3}Zn_{0.7}Fe_2O_4$, $Co_{0.7}Zn_{0.3}Fe_2O_4$ annealed at 400 and 1000 °C.

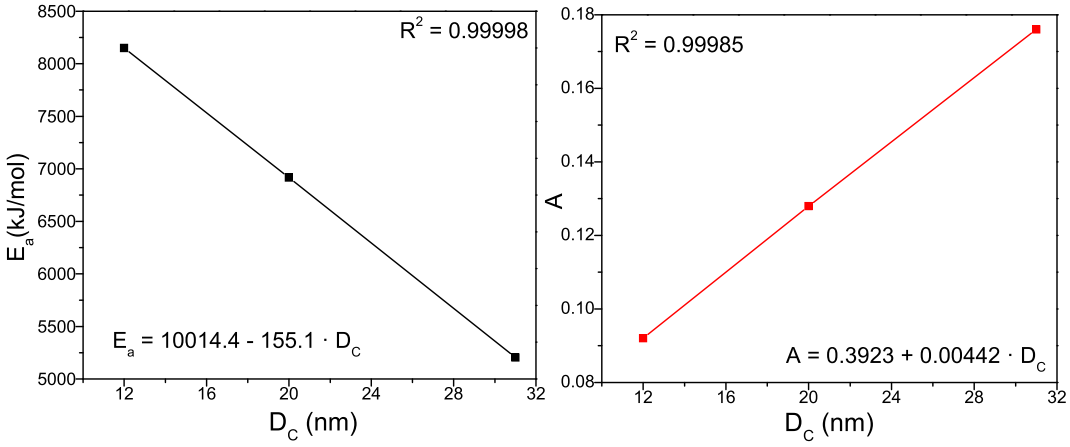

Fig. 6. The dependence of activation energy (Ea), pre-exponential factor (A) and crystallite size (D_C) at 1000 °C.

and to the presence of SiO_2 matrix that strongly influence the NCs structure [33–35].

3.5. SEM and TEM microscopy

Fig. 7 shows the SEM and TEM images, the elemental (Zn, Co, Fe, O, Si) and particles distribution of $ZnFe_2O_4$, $Co_{0.3}Zn_{0.7}Fe_2O_4$ and $Co_{0.7}Zn_{0.3}Fe_2O_4$ annealed at 1000 °C. The SEM images reveal weakly agglomerated, small irregular shape agglomerations with relatively narrow particle size distribution (50–100 nm).

The surface morphology shows a coalescing behaviour of the agglomerated particles, which could be due to interfacial surface tension phenomena [15,36]. SiO_2 embedding acts as a spacer between the nanoparticles and hence reduces agglomeration [19]. TEM images reveal partially agglomerated particles of spherical shape and variable size. According to TEM distribution, the nanoparticles size increases with increasing Co content in ferrite ($ZnFe_2O_4$ (14 nm) > $Co_{0.3}Zn_{0.7}Fe_2O_4$ (24 nm) > $Co_{0.7}Zn_{0.3}Fe_2O_4$ (32 nm)). The TEM images show the particle sizes, without taking into consideration whether they are single-crystal or not [27,36]. In agreement with the elemental distribution map, the intensity of Zn lines decreases, while the intensity of Co lines increases with increasing Co content. The Co/Zn/Fe ratio in ferrites determined by ICP-OES, EDX-SEM and EDX-TEM and the theoretical Co/Zn/Fe ratio together with nanocrystallites size calculated by XRD and nanoparticle size determined by TEM are summarized in Table 2. The measured values are in good agreement with the theoretical values.

3.6. Colour measurements

The ferrite- powders are coloured in dark brown to black shades. The colour representation using CIELAB uniform colour space coordinates (Fig. 8) is represented according to L*, a* and b* Cartesian coordinates or L*, C* and h^o cylindrical coordinates. The L* represents the lightness ranging between L* = 0 (darkest black) and L* = 100 (brightest white), while a* and b* represents the shade and saturation (chromatics), considering true neutral grey values at $a^* = 0$ and $b^* = 0$, where a^* axis represents the green–red component and b^* axis represents the blue–yellow component [37].

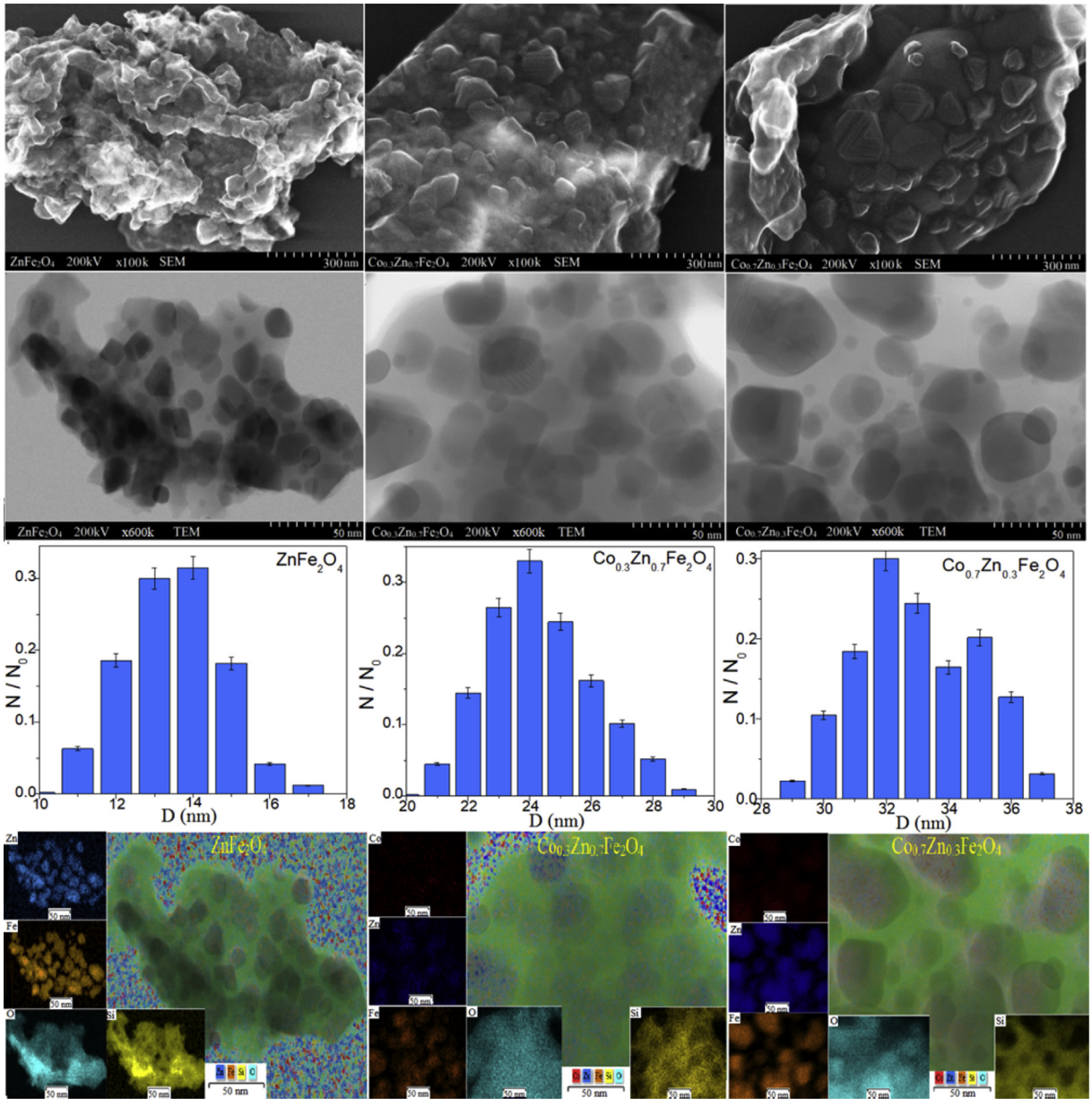

Fig. 7. SEM and TEM images, particle and elemental distribution of $ZnFe_2O_4$, $Co_{0.3}Zn_{0.7}Fe_2O_4$, $Co_{0.7}Zn_{0.3}Fe_2O_4$ annealed at 1000 °C.

Table 2
Theoretical and measured Co/Zn/Fe ratio, nanocrystallites size (D_C) by XRD and nanoparticle size (D) by TEM of $ZnFe_2O_4$, $Co_{0.3}Zn_{0.7}Fe_2O_4$ and $Co_{0.7}Zn_{0.3}Fe_2O_4$ at 1000 °C.

Sample	Co/Zn/Fe ratio				D_C (nm)	D (nm)
	ICP-OES	EDX-SEM	EDX-TEM	Theoretical		
$ZnFe_2O_4$	0/1.04/2.02	0/0.98/2.06	0/1.01/2.00	0.0/1.0/2.0	12	14
$Co_{0.3}Zn_{0.7}Fe_2O_4$	0.29/0.71/2.01	0.32/0.68/2.08	0.30/0.71/2.03	0.3/0.7/2.0	20	24
$Co_{0.7}Zn_{0.3}Fe_2O_4$	0.69/0.31/2.03	0.72/0.28/2.11	0.71/0.30/2.02	0.7/0.3/2.0	31	32

Table 3
CIELAB Cartesian and cylindrical coordinates for the studied ferrites.

Sample	L*	a*	b*	C	h^0
$ZnFe_2O_4$	35.64	5.28	15.9	16.75	71.63
$Co_{0.3}Zn_{0.7}Fe_2O_4$	24.66	1.70	4.10	4.44	67.48
$Co_{0.7}Zn_{0.3}Fe_2O_4$	24.55	1.86	4.78.	5.13	68.74

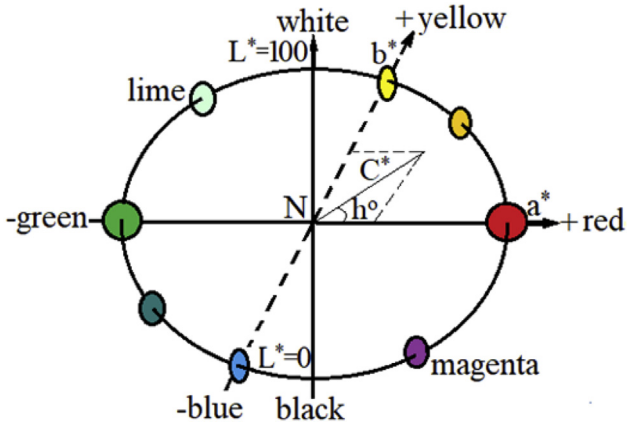

Fig. 8. Cartesian and cylindrical coordinates of CIELAB. In cylindrical coordinates, the colour parameters are calculated with Eqs. (3)–(5) [25]. The measured L*, a* and b* together with C* and h^0 are presented in Table 3. (For interpretation of the references to colour in this figure legend, the reader is referred to the Web version of this article.)

$$L^* = L^* \quad (3)$$

$$C^* = \left(a^{*^2} + b^{*^2}\right)^{1/2} \quad (4)$$

$$h^o = \text{arctg}(b^*/a^*) \quad (5)$$

where L* represents the lightness; C* represents the chromatics, saturation, intensity and purity of colour and h represent the hue, expressed in degrees (0–360°).

The values obtained for a* and b* are positive for all ferrites indicating the colour position in the first quadrant, where the red colour dominates, while the L* values are low, indicating dark colours. The $ZnFe_2O_4$ powder is dark brown due to Fe^{3+} chromophore and has higher L* (35.64) compared to mixed Co-Zn ferrite ($Co_{0.3}Zn_{0.7}Fe_2O_4$ - 24.66 and $Co_{0.7}Zn_{0.3}Fe_2O_4$ - 24.55). The presence of Co decreases the L* values resulting in the increase of darkness, a colour close to back.

The UV-VIS absorption spectra of the ferrite are shown in Fig. 9. In all samples, a maximum absorbance is observed in the range 200–350 nm, with very close values. The $Co_{0.3}Zn_{0.7}Fe_2O_4$ and $Co_{0.7}Zn_{0.3}Fe_2O_4$ have

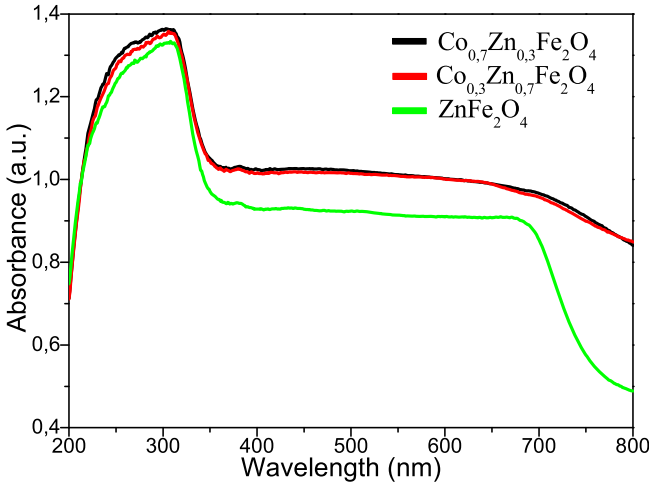

Fig. 9. UV-VIS absorption spectra for $Co_{0.7}Zn_{0.3}Fe_2O_4$, $Co_{0.3}Zn_{0.7}Fe_2O_4$ and $ZnFe_2O_4$.

similar absorption patterns, while $ZnFe_2O_4$ shows a more pronounced decrease in absorbance after 700 nm. At higher temperatures, the systems modification could be related to the elimination of defects (oxygen vacancies) leading to less distorted cationic sites and better-defined colours. Generally, these defects cause distorted tetrahedral/octahedral sites, changes in the ligand field strength/chromophore, which results in the colour change [25]. The obtained results indicate that mixed Zn-Co ferrites can be successfully used as ceramic pigments due to their even, dark brown to black colours and thermal resistance.

4. Conclusions

The $ZnFe_2O_4$, $Co_{0.3}Zn_{0.7}Fe_2O_4$ and $Co_{0.7}Zn_{0.3}Fe_2O_4$ nanoparticles were synthesized by sol-gel method. The thermal analysis and FT-IR spectroscopy confirm the formation of Zn-, Co- and Fe-succinate precursors by the redox reaction between nitrates and 1,4-BD. The thermal analysis showed the formation of ferrites in 3 stages: (*i*) loss of crystallization water, (*ii*) formation of the Zn-, Co- and Fe-succinate precursors and (*iii*) decomposition of the succinate precursors and formation of Zn- and Co-ferrites. The rate constant increases with increasing Co content and decreasing Zn content. The activation energy decreases, while the pre-exponential factor increases with increasing Co content. The FT-IR spectroscopy confirms the formation of succinate precursors and SiO_2 matrix at 200 °C and mixed Zn-Co ferrites at 1000 °C. For gels with low Zn and high Co content ($Co_{0.7}Zn_{0.3}Fe_2O_4$), XRD reveal a single-phase, while for gels with high Zn and low Co content ($ZnFe_2O_4$ and $Co_{0.3}Zn_{0.7}Fe_2O_4$) a main (ferrite) and two secondary (Zn_2SiO_4 and SiO_2) phases appear. The absence of phase transformations after 400 °C in the thermal analysis indicates the samples stability. The similar FT-IR spectra and XRD diffraction patterns of samples annealed at 400 and 1000 °C confirms the thermal stability of samples between 400 and 1000 °C. The increase of nanocrystallite size with increasing Zn substitution with Co: $ZnFe_2O_4$ (12 nm), $Co_{0.3}Zn_{0.7}Fe_2O_4$ (22 nm) and $Co_{0.7}Zn_{0.3}Fe_2O_4$ (31 nm) at 1000 °C and increase of activation energy was observed. The surface morphology revealed well crystallized grains, with relatively homogeneous grain distribution. TEM images reveal partially agglomerated particles of spherical shape with variable size (from 14 to 32 nm) depending on Co content. The SSAs determined by BET method were below 1 m^2/g. The colour measurements and UV–Vis absorption pattern indicate that Co-Zn ferrites, coloured in dark brown to black shades, can be used successfully as ceramic pigments.

Acknowledgments

This work was funded by the Romanian Ministry of Research and

Innovation through Program 1 - Development of the National Research and Development System, Subprogram 1.2 -Institutional Performance-Projects for Financing Excellence in RDI, Contract No. 19PFE/20018 and through CNCS-UEFISCDI PNCDI III mobility grant PN-III-P1-1.1-MC-2018-0816. Also, the authors would like to express their gratitude to Lucian Barbu-Tudoran for the electron microscopy measurements and to Mihaela Lazar for BET measurements.

References

[1] C.A. Charitidis, P. Georgiou, M.A. Koklioti, A.F. Trompeta, V. Markakis, Manufacturing nanomaterials: from research to industry, Manuf. Rev. 1 (2014) 11.
[2] N. Han, P. Liu, J. Jiang, L. Ai, Z. Shao, S. Liu, Recent advances in nanostructured metal nitrides for water splitting, J. Mater. Chem. A. 6 (2018) 19912–19933.
[3] Y. Zhang, S.J. Park, Incorporation of RuO_2 into charcoal-derived carbon with controllable microporosity by CO_2 activation for high-performance supercapacitor, Carbon 122 (2017) 287–297.
[4] Y. Zhang, S.J. Park, Facile construction of MoO_3@ZIF-8 core-shell nanorods for efficient photoreduction of aqueous Cr (VI), Appl. Catal. B Environ. 240 (2019) 92–101.
[5] Y. Zhang, S.J. Park, Bimetallic AuPd alloy nanoparticles deposited on MoO_3 nanowires for enhanced visible-light driven trichloroethylene degradation, J. Catal. 361 (2018) 238–247.
[6] Y. Zhang, S.J. Park, Au–Pd bimetallic alloy nanoparticle-decorated BiPO4 nanorods for enhanced photocatalytic oxidation of trichloroethylene, J. Catal. 355 (2017) 1–10.
[7] K.K. Kefeni, B.B. Mamba, T.A.M. Msagati, Application of spinel ferrite nanoparticles in water and wastewater treatment: a review, Separ. Purif. Technol. 188 (2017) 399–422.
[8] T. Dippong, O. Cadar, E.A. Levei, I.G. Deac, G. Borodi, Formation of $CoFe_2O_4$/PVA-SiO_2 nanocomposites: effect of diol chain length on the structure and magnetic properties, Ceram. Int. 44 (2018) 10478–10485.
[9] T.R. Tatarchuk, N.D. Paliychuk, M. Bououdina, B. Al-Najar, M. Pacia, W. Macyk, A. Shyichuk, Effect of cobalt substitution on structural, elastic, magnetic and optical properties of zinc ferrite nanoparticles, J. Alloys Compd. 731 (2018) 1256–1266.
[10] M. Zamani, E. Naderi, M. Aghajanzadeh, M. Naseri, A. Sharafi, H. Danafar, $Co_{1-x}Zn_xFe_2O_4$ based nanocarriers for dual-targeted anticancer drug delivery: synthesis, characterization and in vivo and in vitro biocompatibility study, J. Mol. Liq. 274 (2019) 60–67.
[11] R. Rani, S.K. Sharma, K.R. Pirota, M. Knobel, Sangeeta Thakur, M. Singh, Effect of zinc concentration on the magnetic properties of cobalt-zinc nanoferrite, Ceram. Int. 38 (2012) 2389–2394.
[12] V.G. Patil, S.E. Shirsath, S.D. More, S.J. Shukla, K.M. Jadhav, Effect of zinc substitution on structural and elastic properties of cobalt ferrite, J. Alloys Compd. 488 (2009) 199–203.
[13] R.R. Powar, V.D. Phadtare, V.G. Parale, H.-H. Park, S. Pathak, P.R. Kamble, P.B. Piste, D.N. Zambare, Structural, morphological, and magnetic properties of $Zn_xCo_{1-x}Fe_2O_4$ ($0 \leq x \leq 1$) prepared using a chemical co-precipitation method, Ceram. Int. 44 (2018) 20782–20789.
[14] C. Singh, S. Jauhar, V. Kumar, J. Singh, S. Singhal, Synthesis of zinc substituted cobalt ferrites via reverse micelle technique involving in situ template formation: a study on their structural, magnetic, optical and catalytic properties, Mater. Chem. Phys. 156 (2015) 188–197.
[15] A.H. El Foulani, A. Aamouche, F. Mohseni, J.S. Amaral, D.M. Tobaldi, R.C. Pullar, Effect of surfactants on the optical and magnetic properties of cobalt-zinc ferrite $Co_{0.5}Zn_{0.5}Fe_2O_4$, J. Alloys Compd. 774 (2019) 1250–1259.
[16] M. Atif, M.W. Asghar, M. Nadeem, W. Khalid, Z. Ali, S. Badshah, Synthesis and investigation of structural, magnetic and dielectric properties of zinc substituted cobalt ferrites, J. Phys. Chem. Solids 123 (2018) 36–42.
[17] J. Lopez, L.F. Gonzalez-Bahamon, J. Prado, J.C. Caicedo, G. Zambrano, M.E. Gomez, J. Esteve, P. Prieto, Study of magnetic and structural properties of ferrofluids based on cobalt-zinc ferrite nanoparticles, J. Magn. Magn. Mater. 324 (2012) 394–402.
[18] M. Sundararajan, L.J. Kennedy, U. Aruldoss, S.K. Pasha, J.J. Vijaya, S. Dunn, Microwave combustion synthesis of zinc substituted nanocrystalline spinel cobalt ferrite: structural and magnetic studies, Mater. Sci. Semicond. Process. 40 (2015) 1–10.
[19] K. Nadeem, M. Shahid, M. Mumtaz, Competing crystallite size and zinc concentration in silica coated cobalt ferrite nanoparticles, Prog. Nat. Sci-Mater. 24 (2014) 199–204.
[20] A. Poorbafrani, E. Kiani, Enhanced microwave absorption properties in cobalt-zinc ferrite based nanocomposites, J. Magn. Magn. Mater. 416 (2016) 10–14.
[21] Y. Zhou, X. Wu, W. Wu, X. Huang, W. Chen, Y. Tian, D. He, Structure and magnetic properties evolution of cobalt-zinc ferrite with lithium substitution, Mater. Sci. Semicond. Process. 41 (2016) 162–167.
[22] T. Dippong, E.A. Levei, O. Cadar, F. Goga, G. Borodi, L. Barbu-Tudoran, Thermal behavior of $Co_xFe_{3-x}O_4/SiO_2$ nanocomposites obtained by a modified sol-gel method, J. Therm. Anal. Calorim. 128 (2017) 39–52.
[23] M. Kubisztal, J. Kubisztal, M. Karolus, K. Prusik, G. Haneczok, Evolution of frozen magnetic state in co-precipitated $Zn_\delta Co_{1-\delta}Fe_2O_4$ ($0 \leq \delta \geq 1$) ferrite nanopowders, J. Magn. Magn. Mater. 454 (2018) 368–374.
[24] P.N. Medeiros, Y.F. Gomes, M.R.D. Bomio, I.M.G. Santos, M.R.S. Silva, C.A. Paskocimas, M.S. Li, F.V. Motta, Influence of variables on the synthesis of $CoFe_2O_4$ pigment by the complex polymerization method, J. Adv. Ceram. 4 (2015) 135–141.
[25] S.J. Moeen, M.R. Vaezi, A.A. Yousefi, Chemical Synthesis of nano-crystalline nickel-zinc ferrite as a magnetic pigment, Prog. Color Colorants Coat. 3 (2010) 9–17.
[26] T. Dippong, F. Goga, Advanced instrumental analysis techniques. Thermal methods, in: Romanian: Tehnici avansate de analiza instrumentala. Metode termice, Risoprint Cluj Napoca, 2016.
[27] T. Dippong, E.A. Levei, O. Cadar, A. Mesaros, G. Borodi, Sol-gel synthesis of $CoFe_2O_4$:SiO_2 nanocomposites - insights into the thermal decomposition process of precursors, J. Anal. Appl. Pyrolysis 125 (2017) 169–177.
[28] A.H. Ashour, A.I. El-Batal, M.I.A. Maksouda, G.S. El-Sayyad, S. Labib, E. Abdeltwab, M.M. El-Okr, Antimicrobial activity of metal-substituted cobalt ferrite nanoparticles synthesized by sol-gel technique, Particuology 40 (2018) 141–151.
[29] B.C. Babu, S. Buddhudu, Analysis of structural and electrical properties of Ni^{2+}: Zn_2SiO_4 ceramic powders by sol–gel method, J. Sol. Gel Sci. Technol. 70 (3) (2014) 405–415.
[30] Joint Committee on Powder Diffraction Standard, International Center for Diffraction Data, 1999.
[31] T. Dippong, O. Cadar, E.A. Levei, C. Leostean, L. Barbu Tudoran, Effect of annealing on the structure and magnetic properties of $CoFe_2O_4$:SiO_2 nanocomposites, Ceram. Int. 43 (2017) 9145–9152.
[32] T. Dippong, O. Cadar, E.A. Levei, I. Bibicu, L. Diamandescu, C. Leostean, M. Lazar, G. Borodi, L. Barbu Tudoran Lucian, Structure and magnetic properties of $CoFe_2O_4$/SiO_2 nanocomposites obtained by sol-gel and post annealing pathways, Ceram. Int. 43 (2017) 2113–2122.
[33] S.Y. Zhao, D.K. Lin, C.W. Kim, I.L.G. Cha, Y.I.I. Kim, Y.S. Kang, Synthesis of magnetic nanoparticles of Fe_3O_4 and $CoFe_2O_4$ and their surface modification by surfactant adsorption, Bull. Korean Chem. Soc. 27 (2006) 237–242.
[34] C.C. Wang, J.M. Lin, C.R. Lin, S.C. Wang, Preparation and application of hollow silica/magnetic nanocomposite, Int. J. Mod. Phys. Conf. Ser. 6 (2012) 601–609.
[35] K. Winiarska, R. Klimkiewicz, W. Tylus, A. Sobianowska-Turek, J. Winiarski, B. Szczygieł, I. Szczygieł, Study of the catalytic activity and surface properties of manganese-zinc ferrite prepared from used batteries, J. Chem. (2019), 5430904.
[36] T.R. Tatarchuk, M. Bououdina, N.D. Paliychuk, I.P. Yaremiy, V.V. Moklyak, Structural characterization and antistructure modeling of cobalt substituted zinc ferrites, J. Alloys Compd. 694 (2017) 777–791.
[37] M.E. Grad, G.M. Simu, S.G. Muntean, A.X. Lupea, Sinteza, caracterizarea si studiul de culoare in spatial color CIELAB ale unor coloranti disazoici simetrici derivati ai acidului 4,4-,diaminostilben-2,2'-disulfonic, Rev. Chim. 58 (2007) 214–217.